Why are Mountaintops Cold? The Decorrelation of Surface Temperature and Elevation Due to the Greenhouse Effect Weakening on Early Mars

Bowen Fan[1], Malte F. Jansen[1], Michael A. Mischna[2], Edwin S. Kite[1]

[1]Department of the Geophysical Sciences, University of Chicago, Chicago, Illinois, 60637, USA
[2]Jet Propulsion Laboratory, California Institute of Technology, Pasadena, CA, 91109, USA

Key Points:

- Surface temperature decorrelates with elevation with a thinner CO_2 atmosphere during Martian history and in climate models.
- The decorrelation is attributed to the weakening of the atmospheric greenhouse effect, rather than atmospheric thickness.
- The decorrelation is accompanied with an atmospheric lapse rate decrease above the low elevations.

Corresponding author: Bowen Fan, bowen27@uchicago.edu

Abstract

The wet-to-dry transition of Mars is recorded by a changing distribution of rivers, which was interpreted as the result of a decorrelation between surface temperature and elevation with a thinner atmosphere. Here we use a climate model to re-examine the interpretation. We find that the weakening of the greenhouse effect, rather than atmospheric pressure, accounts for the decorrelation. The decorrelation happens near surface pressure ~ 0.1 bar for a pure CO_2 atmosphere, or longwave optical depth ~ 1 for a gray gas. Under the weak greenhouse limit, the surface is mainly heated by insolation and thus surface temperature decorrelates with elevation. Under the strong greenhouse limit, the surface is mainly heated by the atmosphere, whose temperature is controlled by advection and convection over the lowlands. Our results suggest that the correlation between river distribution and elevation should be re-examined with different greenhouse forcings and a low atmospheric pressure.

Plain Language Summary

The evolution of Martian climate is linked to a transition in the surface temperature pattern. Snow/ice caps tend to accumulate on mountaintops early in Mars history, but they are located at the poles in the modern era. Previous work suggested that the transition is due to a reduction in air density over geologic time. Here we show that it is, rather, due to a weaker greenhouse effect by using global climate simulations. The transition in global temperature pattern is further linked to the change of the temperature structure. With weaker greenhouse effects, the air above the lowlands cools slower with height. Our work reveals a novel connection between climate and geomorphology, which may work over a broad range of planetary environments.

1 Introduction

The climate of early Mars is not well understood. Mars lost its CO_2-dominated atmosphere over time, from up to 2-bar pressure around 4 Ga to 6 mbar today (Jakosky et al., 2018; Warren et al., 2019). The atmospheric evolution of Mars has been accompanied by climate change, which is recorded by shifts in the spatial distribution of rivers and lakes (Kite, 2019). Consistently, climate models predict shifts in surface temperature pattern with decreasing atmospheric CO_2 (Wordsworth, 2016). When the CO_2 atmosphere is thick, surface temperature, T_s, decreases with elevation (correlated with topography); when the CO_2 atmosphere is thin, T_s only depends on latitude/insolation (decorrelated with topography). Why does the thickness of the CO_2 atmosphere control the pattern of surface temperature?

The distribution of Martian surface temperature has been studied for more than 50 years. Sagan and Pollack (1968) predicted that the variation of surface temperature with elevation should be small on modern Mars and attributed it to a weak greenhouse effect, gentle slopes, and, most importantly, a thinner atmosphere. Recently, Wordsworth (2016) suggested that the decorrelation of surface temperature and elevation ($T_s - Z_s$ decorrelation) from thick-to-thin atmospheres arises because lower air density reduces turbulent heat exchange between the surface and atmosphere. On the other hand, geologic constraints seem to be contradictory about the connection between atmospheric thickness (P_s) and the water flow controlled by surface temperature. Kite (2019) suggests an increased control of fluvial sediment transport by latitude over time due to atmospheric decay from $P_s > 0.3$ bar to $P_s < 0.1$ bar. However, modeling shows that transition of river-flow landforms can also be simulated with a constant, 0.15 bar pressure (Kite et al., 2022). Thus, it remains unclear if, and by what mechanism, P_s controls the T_s distribution throughout geologic time.

In this paper, we will examine under what circumstances surface temperature decorrelates with elevation. We ask: (1) Is there a single variable that can explain the $T_s - Z_s$ decorrelation? Is it atmospheric pressure? (2) What is the critical point for the $T_s - Z_s$ decorrelation? (3) What physical mechanism explains the decorrelation? We introduce our

methodology in Section 2. We present and analyse the simulation results in Section 3. Section 4 includes our conclusion, limitations of this research, and implications for future work on early Mars and other planets.

2 Methods

2.1 Numerical Modeling

We use the MarsWRF General Circulation Model (GCM) (Richardson et al., 2007; Toigo et al., 2012) to investigate the $T_s - Z_s$ decorrelation across different atmospheres. The model resolution is 72×36×40. All simulations are run for 20 years with 5 years of spin up.

To aid understanding, we use idealized simulations with the following simplifications: (1) We consider two options for radiative transfer schemes: a pure CO_2 atmosphere using a correlated-k radiative transfer approach (Mischna et al., 2012), or a gray gas. Under the gray gas scheme, the longwave absorption coefficient, κ, is varied, allowing us to decouple the greenhouse effect from surface pressure. The shortwave scattering and absorption are set to zero. Surface albedo is uniformly 0.2. (2) The planetary obliquity and orbital eccentricity are set to zero, with solar constant 75% of the modern Martian value. (3) The range of mean surface pressure that we consider is between 0.01 bar and 3 bar. (4) Our simulations are performed with either modern Mars topography (blue dashed contours in Fig. 1a & Fig. 1b) or ideal topography (blue dashed contours in Fig. 1d & Fig. 1e). In the main text, the ideal topography is a 6000-km-high, Gaussian-shaped mountain placed at the equator (comparable to Tharsis on Mars). Our results are validated with various ideal topographies (see Supplementary Materials).

2.2 Definition of the orographic temperature control: relative surface lapse rate γ

The relationship between surface temperature, T_s, and elevation, Z_s, is quantified as relative surface lapse rate, γ:

$$\gamma = \frac{1}{\Gamma_a}\frac{dT_s}{dZ_s} \tag{1}$$

where Z_s is surface elevation, and Γ_a is the adiabatic lapse rate. $\frac{dT_s}{dZ_s}$ is quantified by calculating a linear regression of the time-mean model output in the tropical area (see the red dashed lines in Fig. 1b). When T_s is correlated with elevation, the surface lapse-rate is forced to near the atmospheric adiabatic lapse rate, Γ_a, thus γ is close to 100%. When T_s is decorrelated, γ is close to 0.

3 Results

3.1 T_s distributions under different simulations: two limits

Fig. 1 shows how surface temperature distribution and relative surface lapse rate change across different simulations. In all cases, T_s decreases with increasing latitude. Thus, polar regions are global temperature minima, and hence become "cold-traps" to volatiles (Ding & Wordsworth, 2020). This is consistent with our setting obliquity to 0° (polar cold-traps are created by a radiation deficit).

On the other hand, cold-traps can also be created by the topography under some cases. For example, equatorial highlands are cold-traps in the optically thin atmosphere cases (Fig. 1a and Fig. 1b). We confirm that for a CO_2 atmosphere, the orographic control (γ) increases with the thickness of CO_2 (Fig. 1e). Under the thick CO_2 limit, γ is close to 100%. Under the thin CO_2 limit ($P_s \leq 0.1$ bar), γ becomes less than 50%, and the T_s distribution

becomes zonally banded. The trend is independent of the specific shape of the topography (compare red line and blue line in Fig. 1e).

By using gray gas simulations, the effect of CO_2 is further decoupled into a pressure effect and greenhouse effect, which are quantified as surface pressure, P_s, and surface longwave optical depth, τ, respectively. We find that T_s is correlated with elevation (high γ) only under high τ cases, but not under high P_s cases. $\gamma \to 100\%$ when $\tau > 1$. This is true even for very thin atmospheres ($P_s = 0.01$ bar). When τ is fixed, increasing P_s only slightly increases γ if τ is small ($\tau < 0.1$). In conclusion, our results suggest that it is primarily the greenhouse effect, rather than the surface pressure, that controls whether or not the T_s pattern is correlated with elevation.

3.2 Surface energy budgets

According to Wordsworth (2016), atmospheric thickness/pressure is responsible for the decorrelation because of its effect on atmosphere-surface sensible heat exchange. If this hypothesis is correct, then one should expect the role of sensible heat exchange to decrease when P_s decreases. To test this expectation, first we examine the surface energy budget in our simulations. In our model, the surface energy budget is:

$$SW + LW_a = LW_s + SH \tag{2}$$

where SW is the net shortwave heating from the Sun, LW_a is the longwave heating from the atmosphere (greenhouse effect), LW_s is the longwave cooling by surface emission, and SH is the cooling by sensible heat flux, respectively. There is no latent heat term because water vapor and CO_2 condensation are disabled in our idealized simulations.

To visualize the model output, we perform a tropical meridional average (20° N - 20° S) and time average on the model output. With this approach, the temperature gradient due to solar insolation is minimized, and the annual mean longitudinal variation in T_s distribution is depicted by the LW_s term. For example, the red line in Fig. 2a indicates a temperature minimum at longitude = 0° in the tropics, which corresponds to the highland in our ideal topography (Fig. 1b & Fig. 1d).

The results for the surface energy budget in Fig. 2 show that surface sensible heat flux (SH, blue lines) has generally relatively little zonal variation and is hence unable to balance the zonally varying surface emissions (LW_s, red lines) that arise from variations in T_s under optically thick atmospheres. Instead, zonal variations in LW_s are primarily balanced by opposite variations in greenhouse heating (LW_a, cyan lines). As the atmospheric longwave optical thickness decreases, LW_a becomes increasingly weak and thus becomes unable to balance zonally varying surface emissions LW_s. Eventually, LW_s becomes close to the shortwave absorption (SW, blue lines). The controlling role of LW_a does not change by switching the CO_2 radiation to a gray gas scheme with fixed surface pressure, or switching to other topographies (Supplementary Fig. 1).

The results in Fig. 2 indicate that zonally varying surface temperatures require effective radiative coupling between the surface and the atmosphere, which, in turn, requires high longwave optical thickness. This leaves the question why surface sensible heat flux, SH, cannot play a similar role. From the atmospheric perspective, the atmospheric energy budget places an upper limit on SH. In a globally averaged sense, the atmospheric energy balance is between radiative cooling, $\overline{R_a}$, and sensible heating, $\overline{SH}$:

$$\overline{R_a} = \overline{SH} \tag{3}$$

where the overbar denotes a horizontal average. Under the optically thin limit, $\overline{R_a}$ becomes small, thus placing an upper limit on $\overline{SH}$. Locally, large SH variations with topography would then require large negative SH in the lowlands, which is not likely to happen as a near-surface inversion stabilizes the boundary layer and suppresses turbulent heat exchange.

In summary, with a low greenhouse effect (i.e., low atmospheric emissivity), atmospheric emission back to the surface, LW_a, is negligible. As a result, the surface energy balance becomes dominated by a balance between insolation, SW, and surface emission, LW_s, such that T_s (which regulates LW_s) is purely set by solar insolation and becomes independent of elevation. With a strong greenhouse effect, atmospheric radiation LW_a becomes important in the surface energy balance, with the leading balance eventually being between surface emission LW_s and LW_a. The surface temperature, hence, is controlled by the atmospheric temperature, which, in turn, varies height.

3.3 Atmospheric temperature structure

In the previous section, we showed that radiative coupling links the surface temperature distribution to the atmospheric temperature. Assuming an approximately linear lapse rate, Γ, surface temperature T_s can be expressed as:

$$T_s = T_a + \Gamma(Z_a - Z_s) \tag{4}$$

where T_a is atmospheric temperature at height Z_a. Given a fixed Z_a, two ingredients are necessary for the surface temperature T_s to follow an adiabat with Z_s: (1) the same T_a at Z_a (i.e., a weak temperature gradient; Sobel et al., 2001); (2) Γ is adiabatic. Thus, a change in the structure of T_s could be due to either a transition of in the horizontal gradient of T_a, or a transition of Γ, or both.

Atmospheric temperature structures with changing greenhouse effects are shown in Fig. 3. Under the strong greenhouse limit, the atmosphere is close to isothermal horizontally and adiabatic vertically (Fig. 3a & Fig. 3c). Under the weak greenhouse limit, the upper atmosphere remains horizontally isothermal, while the air columns above the lowlands are partially stably stratified (Fig. 3b & Fig. 3d). Thus, the transition in T_s can be better explained by the deviation from an adiabat over the lowlands.

Why does the vertical structure deviate from the adiabat for weak greenhouse effects? For the weak greenhouse limit, T_s is close to uniform due to the surface energy budget constraint discussed above. However, the atmosphere above the lowlands is warmed by heat advection from the highlands, which stabilizes the lapse rate (Fig. 4b & 4d, compare red lines and red crosses). In contrast, the air above the highlands is cooled by the circulation thus the air column is convective and adiabatic.

4 Discussion and Summary

On Earth, mountaintops are cold and the surface temperature follows the atmospheric lapse rate along the topography, while a transition on Mars eventually led to the decorrelation of T_s with elevation today. Using MarsWRF GCM simulations, we find the decorrelation is controlled by the greenhouse effect. The decorrelation happens near $P_s \sim 0.1$ bar for a pure CO_2 atmosphere, or optical depth $\tau \sim 1$ for a gray gas. The control of the greenhouse effect can be understood as a transition in surface energy budget (Fig. 4). When the greenhouse effect is weak, the surface is uniformly heated by solar insolation, which does not depend on elevation. When the greenhouse effect is strong, the combination of convection (which sets the lapse rates to adiabats) and weak horizontal temperature gradient in the atmosphere is responsible for the adiabatic surface lapse rate. When the greenhouse effect is weak, the atmospheric lapse rate above the lowlands becomes small due to heat advection from the highlands.

There are several limitations to our work: (1) Ice-albedo effects are not included. Surface ice or snow can form at high altitudes in the tropical area when the temperature is cold (e.g., Mount Kilimanjaro on Earth). The high albedo of ice decreases net solar heating. Since the surface temperature structure is controlled by the solar heating under the weak greenhouse limit, our conclusion may not apply across the snowline. (2) Our simulations do

not include other greenhouse gases (e.g., H_2O, H_2). The gray scheme may not adequately capture the radiaitve properties of a CO_2+H_2O or CO_2+H_2 atmosphere across different atmospheric thicknesses and compositions. (3) Topographies with extremely small areas of highlands or lowlands are not simulated, but we think these scenarios are geologically unrealistic on early Mars.

Keeping these limitations in mind, our theory can be applied to GCMs and compared to geologic constraints. Since, according to our results, the surface temperature decorrelation is primary due to the decline of the greenhouse effect, changes in Martian fluvial patterns may arise from non-CO_2 greenhouse gases, rather than the loss of a CO_2-dominated atmosphere (Kite et al., 2022). Compared to the traditional two end-member options for the climate of early Mars: "high T_s + high P_{CO2}" or "low T_s + low P_{CO2}" (Hauber et al., 2008; Fassett et al., 2010; Head et al., 2022), our results suggest a 3rd option (high T_s + low P_{CO2}). Snow and ice caps tend to accumulate at mountaintops under this regime (topographic cold-traps). The snow and ice can be the source of water flow once the ice is melted by seasonal/diurnal heating maxima (Wordsworth et al., 2015; Palumbo et al., 2018; Kite et al., 2022). Future work should focus on the correlation between river locations and elevation with other greenhouse forcings and low atmospheric pressure.

This study is also applicable to the habitability of exoplanets. For rocky planets near the outer edge of their habitable zone, cold-traps created by radiation (e.g., polar regions; permanent nightside for tidally-locked planets) and atmospheric circulation have been proposed (Ding & Wordsworth, 2020). Our work indicates cold-traps can be created by topography when the greenhouse effect is strong. Yet, most exoplanet GCMs assume no topography. Future work should focus on different potential climate regimes under the competition of these cold-traps, as well as their influences on the hydrological cycle and long-term planetary evolution (e.g., the transition between snowball and habitable climates).

Acknowledgments

This research was funded by NASA (80NSSC20K0144+80NSSC18K1476) and NSF award AGS-2033467. Most simulations were completed with resources provided by the University of Chicago Research Computing Center (RCC). A portion of this work was carried out at the Jet Propulsion Laboratory, California Institute of Technology, under a contract with the National Aeronautics and Space Administration (80NM0018D0004).

Open Research

Data necessary to reproduce the figures in this paper is publicly available from the repository Knowledge@UChicago (https://doi.org/10.6082/uchicago.4934) or by emailing the lead author. The MarsWRF source code can be made available by Aeolis Research pending scientific review and a completed Rules of the Road agreement.

References

Ding, F., & Wordsworth, R. D. (2020). Stabilization of dayside surface liquid water via tropopause cold trapping on arid slowly rotating tidally locked planets. *The Astrophysical Journal Letters*, *891*(1), L18.

Fassett, C. I., Dickson, J. L., Head, J. W., Levy, J. S., & Marchant, D. R. (2010). Supraglacial and proglacial valleys on Amazonian Mars. *Icarus*, *208*(1), 86-100.

Hauber, E., van Gasselt, S., Chapman, M. G., & Neukum, G. (2008). Geomorphic evidence for former lobate debris aprons at low latitudes on Mars: Indicators of the Martian paleoclimate. *Journal of Geophysical Research (Planets)*, *113*(E2), E02007.

Head, J. W., Wordsworth, R. D., & Fastook, J. L. (2022). When did Mars become bipolar? Outstanding issues in a conceptual model of a Noachian-Amazonian climate transition from an altitude-dominant temperature environment (ADD) to a latitude-dominant

temperature environment (LDD). *LPSC 2022*, *2678*, 2083.

Jakosky, B. M., Brain, D., Chaffin, M., Curry, S., Deighan, J., Grebowsky, J., ... Zurek, R. (2018). Loss of the Martian atmosphere to space: Present-day loss rates determined from MAVEN observations and integrated loss through time. *Icarus*, *315*, 146-157.

Kite, E. S. (2019). Geologic constraints on early Mars climate. *Space Science Reviews*, *215*(1), 10.

Kite, E. S., Mischna, M. A., Fan, B., Morgan, A. M., Wilson, S. A., & Richardson, M. I. (2022). Changing spatial distribution of water flow charts major change in Mars' greenhouse effect. *Science Advances*, *8*(21), eabo5894.

Mischna, M. A., Lee, C., & Richardson, M. (2012). Development of a fast, accurate radiative transfer model for the Martian atmosphere, past and present. *Journal of Geophysical Research (Planets)*, *117*(E10), E10009.

Palumbo, A. M., Head, J. W., & Wordsworth, R. D. (2018). Late Noachian icy highlands climate model: Exploring the possibility of transient melting and fluvial/lacustrine activity through peak annual and seasonal temperatures. *Icarus*, *300*, 261–286.

Richardson, M. I., Toigo, A. D., & Newman, C. E. (2007). PlanetWRF: A general purpose, local to global numerical model for planetary atmospheric and climate dynamics. *Journal of Geophysical Research (Planets)*, *112*(E9), E09001.

Sagan, C., & Pollack, J. B. (1968). Elevation Differences on Mars. *Journal of Geophysical Research*, *73*, 1373.

Sobel, A. H., Nilsson, J., & Polvani, L. M. (2001). The weak temperature gradient approximation and balanced tropical moisture waves. *Journal of Atmospheric Sciences*, *58*(23), 3650-3665.

Toigo, A. D., Lee, C., Newman, C. E., & Richardson, M. I. (2012). The impact of resolution on the dynamics of the martian global atmosphere: Varying resolution studies with the MarsWRF GCM. *Icarus*, *221*(1), 276-288.

Warren, A. O., Kite, E. S., Williams, J.-P., & Horgan, B. (2019). Through the thick and thin: New constraints on Mars paleopressure history 3.8–4 Ga from small exhumed craters. *Journal of Geophysical Research: Planets*, *124*(11), 2793-2818.

Wordsworth, R. D. (2016). The climate of early Mars. *Annual Review of Earth and Planetary Sciences*, *44*(1), 381-408.

Wordsworth, R. D., Kerber, L., Pierrehumbert, R. T., Forget, F., & Head, J. W. (2015). Comparison of "warm and wet" and "cold and icy" scenarios for early Mars in a 3-D climate model. *Journal of Geophysical Research: Planets*, *120*(6), 1201–1219.

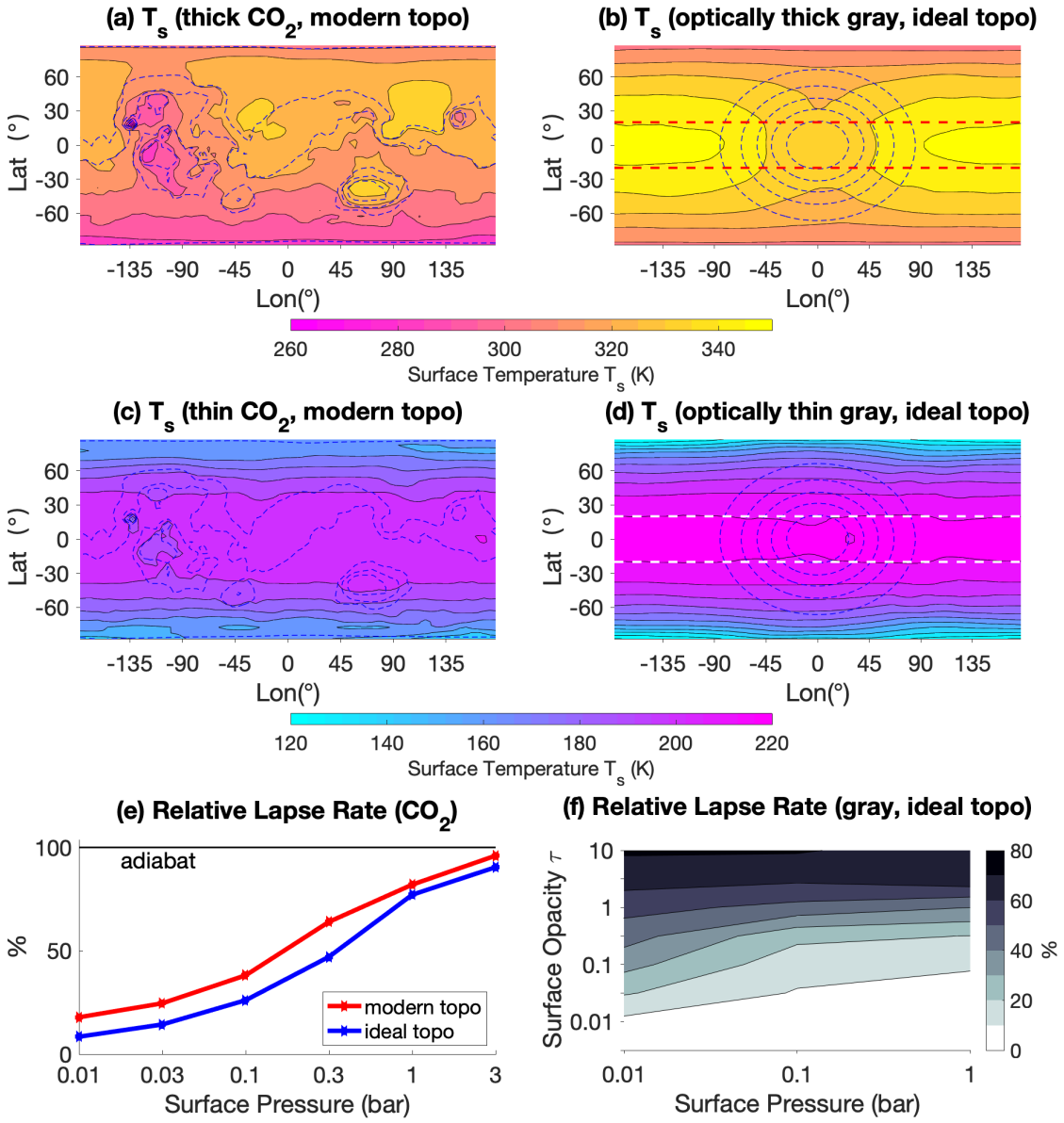

Figure 1. Example of annual mean surface temperature (T_s) patterns and relative surface lapse rates (γ) under different atmospheres. (a) T_s distribution (filled contours) for the case with a 3-bar CO_2 atmosphere and modern Mars topography (blue dashed lines). The topography is plotted with a contour interval of 3000 m from -6000 m to 6000 m, indicating the Tharsis Plateau (-120° lon, 0° lat) and Hellas Basin (60° lon, -30° lat). (b) Same as (a), but for the case with a 1-bar gray gas atmosphere, global mean surface optical depth $\tau = 10$, and ideal topography. The horizontal red dashed lines indicate the zone for tropical averaging in Fig. 2. The ideal topography is a 6000-km-high, Gaussian-shaped mountain placed at the equator, and is plotted with a contour interval of 1000 m from 0 m to 5000 m. (c) Same as (a), but for the case with a 0.01-bar CO_2 atmosphere and modern Mars topography. (d) Same as (b), but for the case with a 1-bar gray gas atmosphere, $\tau = 0.01$, and ideal topography. (e) Relative surface lapse rate (γ) as a function of the thickness of a pure CO_2 atmosphere. (f) γ as a function of atmospheric thickness P_s and surface optical depth τ for cases with gray gas scheme and ideal topography. Note that the pressure effect and the greenhouse effect are decoupled with the gray gas scheme. The data is sampled on a regular grid with $\tau = 0.0003, 0.01, 0.1, 0.3, 1, 3, 10$ and $P_s = 0.01, 0.1, 1$ bar.

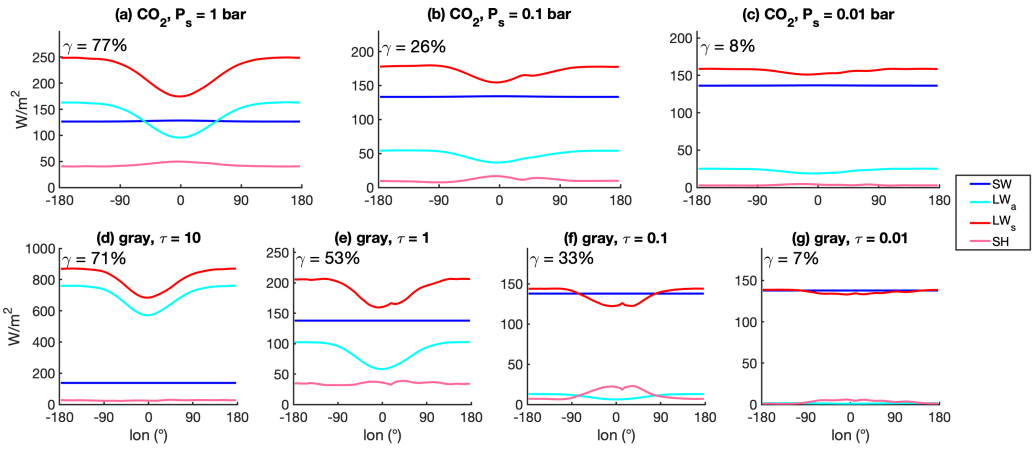

Figure 2. Time-averaged surface energy budgets for simulations with ideal topography and (a-c) CO_2 atmospheres or (d-g) 1-bar gray atmospheres. Surface lapse rate, γ, for each case is indicated in the upper-left corner. SW is the net shortwave heating from the Sun, LW_a is the longwave heating from the atmospheric greenhouse effect, LW_s is the longwave cooling by surface emission, and SH is the cooling by sensible heat flux, respectively. Each term is averaged within the tropics (20°N - 20°S). A dip in the red curve indicates a correlation between T_s and topography (lower T_s, thus lower emission over the mountain), which is controlled by the decrease of greenhouse heating.

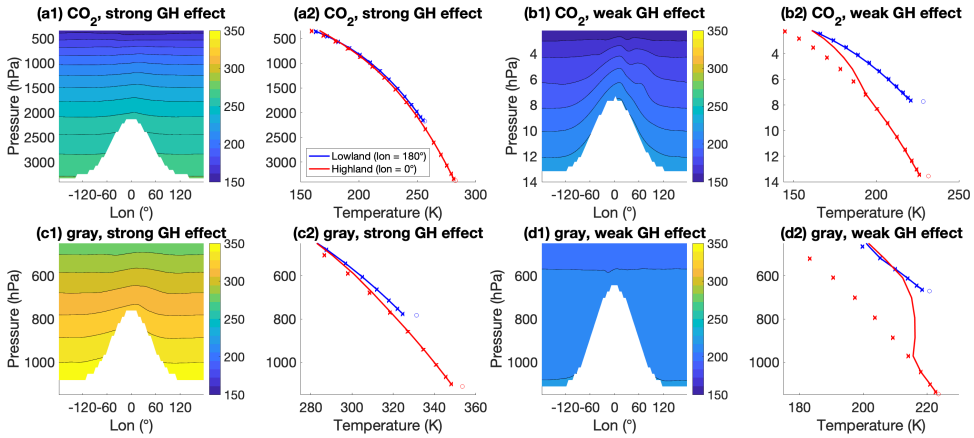

Figure 3. Contour panels: Time-average, equatorial cross-sections of atmospheric temperature T_a for the simulations with ideal topography (see Fig. 1b). Line plots: Time-average vertical thermal structure above the equatorial highlands (blue, lon = 0°) and lowlands (red, lon = 180°) for simulations with ideal topography. Circles, solid lines, and crosses correspond to surface temperature, atmospheric temperature, and adiabats, respectively. The cases are (a) 3-bar CO_2, (b) 0.01-bar CO_2, (c) 1-bar gray gas with $\tau = 10$, (d) 1-bar gray gas with $\tau = 0.01$.

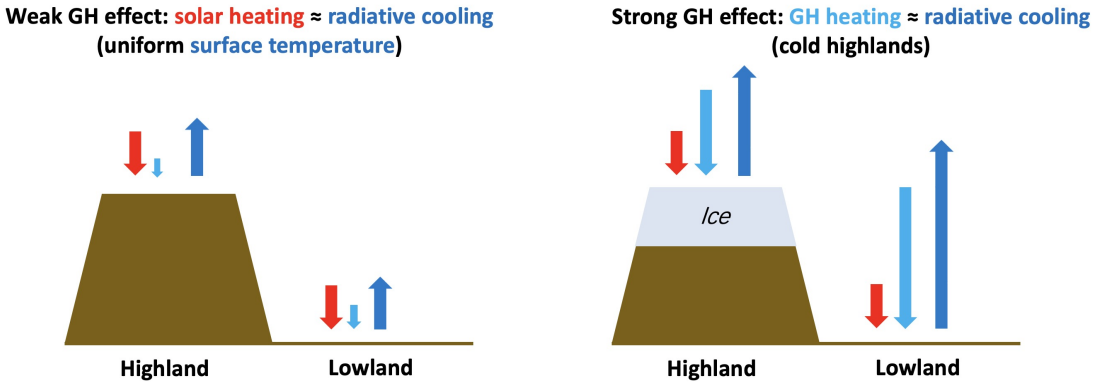

Figure 4. Cartoon diagram showing the mechanism of the transition, from approximately uniform surface temperature to orographically-controlled surface temperature with increasing greenhouse effect. Different arrows indicate different energy fluxes (red: absorbed solar insolation SH; cyan: downward atmospheric emission LW_a; blue: surface emission LW_s). "Ice" indicates the preferred location for water ice accumulation.